Inorganic Chemistry

Article

pubs.acs.org/IC

Flexible Coordination Polymers Composed of Luminescent Ruthenium(II) Metalloligands: Importance of the Position of the Coordination Site in Metalloligands

Atsushi Kobayashi,*[,†,‡] Tadashi Ohba,[†] Erika Saitoh,[†] Yui Suzuki,[†] Shin-ichiro Noro,[§] Ho-Chol Chang,[⊥] and Masako Kato*[,†]

[†]Department of Chemistry, Faculty of Science, Hokkaido University, North-10 West-8, Kita-ku, Sapporo 060-0810, Japan

[‡]Japan Science and Technology Agency (JST), Precursory Research for Embryonic Science and Technology (PRESTO), Kawaguchi, Saitama 332-0012, Japan

[§]Research Institute for Electronic Science, Hokkaido University, North-20, West-10, Kita-ku, Sapporo 001-0020, Japan

[⊥]Department of Applied Chemistry, Faculty of Science and Engineering, Chuo University, 1-13-27 Kasuga, Bunkyo-ku, Tokyo 112-8551, Japan

Supporting Information

ABSTRACT: Coordination polymerization reactions between ruthenium(II) metalloligands $[Ru(n,n'\text{-dcbpy})]^{4-}$ ([***n*Ru**]; n = 4, 5; n,n'-dcbpy = n,n'-dicarboxy-2,2′-bipyridine) and several divalent metal salts in basic aqueous solutions afforded porous luminescent complexes formulated as $[Mg(H_2O)_6]\{[Mg(H_2O)_3][4Ru]\cdot 4H_2O\}$ (**Mg_2[4Ru]·13H_2O**), $[Mg_2(H_2O)_9][5Ru]\cdot 10H_2O$ (**Mg_2[5Ru]·19H_2O**), $\{[Sr_4(H_2O)_9][4Ru]_2\cdot 9H_2O\}$ (**Sr_2[4Ru]·9H_2O**)$_2$, $\{[Sr_2(H_2O)_8][5Ru]\cdot 6H_2O\}$ (**Sr_2[5Ru]·14H_2O**), and $\{[Cd_2(H_2O)_2][5Ru]\cdot 10H_2O\}$ (**Cd_2[5Ru]·12H_2O**). Single-crystal X-ray structural analyses revealed that the divalent metal ions were commonly coordinated by the carboxyl groups of the [***n*Ru**] metalloligand, forming porous frameworks with a void fraction varying from 11.4% **Mg_2[4Ru]·13H_2O** to 43.9% **Cd_2[5Ru]·12H_2O**. **M_2[4Ru]·*n*H_2O** showed a reversible structural transition accompanied by water and methanol vapor adsorption/desorption, while the porous structures of **M_2[5Ru]·*n*H_2O** were irreversibly collapsed by the removal of crystal water. The triplet metal-to-ligand charge-transfer emission energies of **M_2[4Ru]·*n*H_2O** were lower than those of [**4Ru**] in aqueous solution, whereas those of **M_2[5Ru]·*n*H_2O** were close to those of [**5Ru**] in aqueous solution. These results suggested that the position of the coordination site in the metalloligand played an important role not only on the structure of the porous framework but also on the structural flexibility involving the guest adsorption/desorption properties.

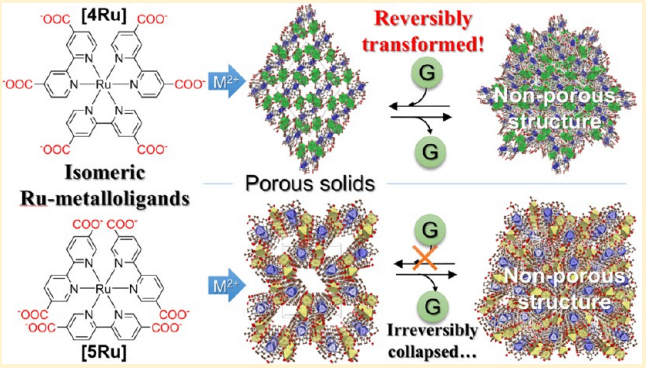

INTRODUCTION

Porous coordination polymers (PCPs) or metal−organic frameworks (MOFs) have drawn considerable attention in recent decades because of their controllable porous frameworks,[1] interesting gas and vapor adsorption properties,[2] and catalytic activity,[3] among other properties.[4] Until now, various metal ions and organic bridging ligands have been utilized to achieve a larger surface area and/or diameter of the porous channels,[5] to enhance the host−guest interaction,[6] and to introduce a catalytic center in the porous frameworks.[3,7] Some PCPs show structural transitions accompanied with guest adsorption/desorption,[8] derived from the moderate coordination bond strength of metal ions. The variable coordination environment of the metal ions is one of the most important characteristic features of PCPs compared to other porous materials. Therefore, interesting physical properties based on the designable porous framework of PCPs by the selection/modification of the metal ion and/or organic ligand are possible. In addition, a powerful method to introduce new functionalities to PCPs is to utilize metal complexes as the bridging ligands.[9−11] For instance, Kitaura et al. reported on PCPs with coordinatively unsaturated metal centers fabricated from metallo Schiff bases, with $[M(salphdc)]^{2-}$ [M = Ni^{2+}, Cu^{2+}; H_4salphdc = N,N'-phenylenebis(salicylideneimine)-dicarboxylic acid] as the metalloligand.[10]

From the viewpoint of versatility regarding the physical properties, $[M(bpy)_3]^{n+}$ (M = Fe, Co, Ru, etc.; bpy = 2,2′-bipyridine) complexes and their derivatives are some of the most fascinating building blocks to construct multifunctional

Received: October 24, 2013
Published: February 21, 2014

PCPs. This is because of their interesting properties, including photoluminescence,[12] reversible redox activities,[13] spin-crossover properties,[14] and O_2- and H_2-evolving catalytic activities.[15] Several examples have recently been reported by Lin and coworkers; they demonstrated several interesting photocatalytic activities and energy-transfer dynamics in ruthenium(II) and osmium(II) metalloligand based MOFs.[11] Generally, most photophysical phenomena are known to be sensitive to the environment of the functional molecule (e.g., solvent, temperature, and existence of a quencher). Thus, incorporating photofunctional molecules into flexible PCPs may be a promising method to develop new environmentally responsive materials with high sensitivity.

We recently reported on cobalt(III) metalloligand based PCPs, $\{Ln[Co(4,4'\text{-dcbpy})_3]\}$ (Ln = La^{3+}, Nd^{3+}, Gd^{3+}; 4,4′-H_2dcbpy = 4,4′-dicarboxy-2,2′-bipyridine) and found that the porous frameworks are flexible enough to allow the transformation of their crystal structures when accompanied by guest adsorption/desorption.[16] In this work, we chose a similar tris(bipyridyl)-type ruthenium(II) metalloligand bearing six carboxyl groups in one molecule, $[Ru(n,n'\text{-dcbpy})_3]^{4-}$ (Scheme 1; n = 4, 5; [**4Ru**], [**5Ru**]), as the photofunctional building

Scheme 1. Structure Representations of Isomeric Ruthenium(II) Metalloligands [4Ru] and [5Ru]

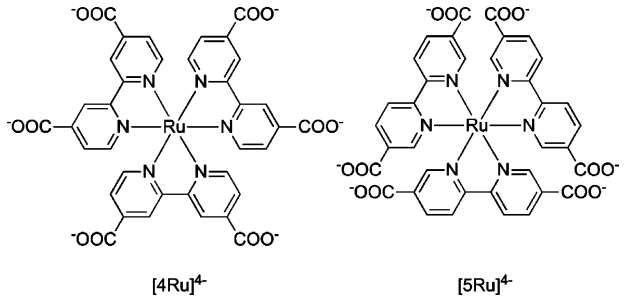

block to introduce new photofunctions into such flexible PCP systems. Alkaline-earth and the zinc group metal ions were selected for coordination polymerization reactions because of their closed-shell d^0 or d^{10} electronic configurations that retain the emission properties of the ruthenium(II) metalloligands. In addition, the various coordination modes of larger metal ions such as Sr^{2+} and Cd^{2+} may be able to contribute to the construction of flexible PCPs. Herein, we report on the syntheses, crystal structures, luminescence properties, and vapor-induced reversible structural transitions of new luminescent PCPs formulated as $[Mg(H_2O)_6]\{[Mg(H_2O)_3][4Ru]\}\cdot 4H_2O$ (**Mg_2[4Ru]·13H_2O**), $[Mg_2(H_2O)_9][5Ru]\cdot 10H_2O$ (**Mg_2[5Ru]·19H_2O**), $\{[Sr_4(H_2O)_9][4Ru]_2\cdot 9H_2O\}$ (**Sr_2[4Ru]·9H_2O**)$_2$, $\{[Sr_2(H_2O)_8][5Ru]\cdot 6H_2O\}$ (**Sr_2[5Ru]·14H_2O**), and $\{[Cd_2(H_2O)_2][5Ru]\cdot 10H_2O\}$ (**Cd_2[5Ru]·12H_2O**). In addition, we demonstrate that the structural flexibilities of these PCPs are strongly dependent on the position of the carboxyl group in the metalloligand.

EXPERIMENTAL SECTION

Syntheses. All starting materials—$RuCl_3\cdot 3H_2O$, $Mg(NO_3)_2\cdot 6H_2O$, $Mg(CH_3COO)_2\cdot 4H_2O$, $SrCl_2\cdot 6H_2O$, $Cd(NO_3)_2\cdot 4H_2O$, 5,5′-dimethyl-2,2′-bipyridine, and 4-methylpyridine—were used as received from commercial sources. Solvents were used without any further purification. Unless otherwise stated, all reactions were performed in air. Ruthenium(II) metalloligands—$[Ru(4,4'\text{-Hdcbpy})_3]$ and $[Ru(5,5'\text{-Hdcbpy})_3]$—were prepared according to published methods.[17,18] Elemental analysis was performed at the analysis center of Hokkaido University.

*Synthesis of $[Mg(H_2O)_6]\{[Mg(H_2O)_3][4Ru]\cdot 4H_2O\}$ (**Mg_2[4Ru]·13H_2O**).* $[Ru(4,4'\text{-Hdcbpy})_3]$ (25 mg, 30 μmol) was dissolved in a mixed solution of triethanolamine (0.075 mL) and water (3 mL). To the resulting clear red solution was slowly diffused in a straight glass tube at 323 K an EtOH solution (5 mL) of $Mg(CH_3COO)_2\cdot 4H_2O$ (21.1 mg, 100 μmol). Red single crystals of **Mg_2[4Ru]·13H_2O** were obtained after 10 days. The crystals were collected by filtration, washed with a small amount of water, and then dried in air for 1 day to afford **Mg_2[4Ru]·13H_2O** (28.4 mg) in 91% yield based on $[Ru(4,4'\text{-Hdcbpy})_3]$. Elem anal. Calcd. for $C_{36}H_{18}N_6O_{12}RuMg_2\cdot 13H_2O$: C, 38.94; H, 3.99; N, 7.57. Found: C, 38.84; H, 4.19; N, 7.51. IR (KBr, cm^{-1}): 3367 s, 1596 s, 1542 s, 1434 m, 1407 m, 1380 s, 1292 w, 1262 w, 1235 m, 1160 w, 1130 w, 1025 w, 908 w, 877 w, 780 m, 699 m, 459 w, 417 w.

Synthesis of $\{[Sr_4(H_2O)_9][4Ru]_2\cdot 9H_2O\}$ $[(Sr_2[4Ru]\cdot 9H_2O)_2]$. $[Ru(4,4'\text{-Hdcbpy})_3]$ (25 mg, 30 μmol) was dissolved in a mixed solution of triethanolamine (0.075 mL) and water (3 mL). To the resulting clear red solution was slowly diffused in a straight glass tube at 323 K an EtOH solution (5 mL) of $SrCl_2\cdot 6H_2O$ (26.3 mg, 100 μmol). Red single crystals of **Sr_2[4Ru]·9H_2O** were obtained after 10 days. The crystals were collected by filtration, washed with a small amount of water, and then dried in air for 1 day to afford **Sr_2[4Ru]·9H_2O** (28.7 mg) in 96% yield based on $[Ru(4,4'\text{-Hdcbpy})_3]$. Elem anal. Calcd for $C_{36}H_{18}N_6O_{12}RuSr_2\cdot 9H_2O$: C, 37.11; H, 3.11; N, 7.21. Found: C, 37.10; H, 3.22; N, 7.49. IR (KBr, cm^{-1}): 3400 m, 2360 w, 2330 w, 1601 s, 1543 m, 1430 w, 1406 m, 1380 s, 1296 w, 1235 w, 1033 w, 915 w, 862 w, 788 m, 709 w, 671 w, 448 w.

*Synthesis of $[Mg_2(H_2O)_9][5Ru]\cdot 10H_2O$ (**Mg_2[5Ru]·19H_2O**).* $[Ru(5,5'\text{-Hdcbpy})_3]\cdot 3H_2O$ (16.6 mg, 19 μmol) was dissolved in a mixed solution of triethanolamine (2 mL) and water (50 μL). To the resulting clear orange-red solution was slowly diffused in a straight glass tube at 298 K an EtOH solution (0.5 mL) of $Mg(NO_3)_2\cdot 6H_2O$ (15.2 mg, 60 μmol). Red single crystals of **Mg_2[5Ru]·19H_2O** were obtained after a few days. The crystals were collected by filtration and washed with a small amount of EtOH to afford **Mg_2[5Ru]·19H_2O** (10.0 mg) in 41% yield based on $[Ru(5,5'\text{-Hdcbpy})_3]$. Elem anal. Calcd for $C_{36}H_{18}N_6O_{12}RuMg_2\cdot 19H_2O$: C, 35.48; H, 4.63; N, 6.90. Found: C, 35.07; H, 4.27; N, 6.98. IR (KBr, cm^{-1}): 3324 w, 1616 s, 1586 s, 1557 s, 1481 m, 1384 s, 1169 m, 1135 m, 1051 m, 842 m, 779 m, 704 m.

*Synthesis of $\{[Sr_2(H_2O)_8][5Ru]\cdot 6H_2O\}$ (**Sr_2[5Ru]·14H_2O**).* $[Ru(5,5'\text{-Hdcbpy})_3]\cdot 3H_2O$ (50.0 mg, 57 μmol) was dissolved in a mixed solution of triethanolamine (150 μL) and water (6 mL). To the resulting clear orange-red solution was slowly diffused in a straight glass tube at 323 K an EtOH solution (6 mL) of $SrCl_2\cdot 6H_2O$ (42.0 mg, 198 μmol). Red single crystals of **Sr_2[5Ru]·14H_2O** were obtained after a few days. The crystals were collected by filtration, washed with a small amount of EtOH, and then dried in air for 1 day to afford **Sr_2[5Ru]·14H_2O** (55.6 mg) in 97% yield based on $[Ru(5,5'\text{-Hdcbpy})_3]$. Elem anal. Calcd for $C_{36}H_{18}N_6O_{12}RuSr_2\cdot 14H_2O$: C, 34.45; H, 3.69; N, 6.70. Found: C, 34.54; H, 3.69; N, 6.68. IR (KBr, cm^{-1}): 3374 w, 1612 s, 1586 s, 1553 s, 1486 s, 1380 s, 1172 m, 1133 m, 1039 m, 933 m, 850 m, 780 m, 707 m.

*Synthesis of $\{[Cd_2(H_2O)_2][5Ru]\cdot 10H_2O\}$ (**Cd_2[5Ru]·12H_2O**).* $[Ru(5,5'\text{-Hdcbpy})_3]\cdot 3H_2O$ (50.0 mg, 56 μmol) was dissolved in a mixed solution of triethanolamine (50 μL) and water (6 mL). To the resulting clear orange-red solution was slowly diffused in a straight glass tube at 298 K an EtOH solution (6 mL) of $Cd(NO_3)_2\cdot 6H_2O$ (68.2 mg, 198 μmol). Red single crystals of **Cd_2[5Ru]·12H_2O** were obtained after a few days. The crystals were collected by filtration, washed with a small amount of EtOH, and then dried in air for 1 day to afford **Cd_2[5Ru]·12H_2O** (18.2 mg) in 25.6% yield based on $[Ru(5,5'\text{-Hdcbpy})_3]$. Elem anal. Calcd for $C_{36}H_{18}N_6O_{12}RuCd_2\cdot 12H_2O$: C, 34.08; H, 3.34; N, 6.62. Found: C, 34.16; H, 3.22; N, 7.09. IR (KBr, cm^{-1}): 3385 w, 1612 s, 1589 s, 1554 s, 1484 m, 1375 s, 1164 m, 1130 m, 1037 m, 832 m, 849 m, 776 m, 707 m.

Photophysical Measurements. The UV−vis adsorption spectrum of each complex was recorded on a Shimadzu UV-2400PC

dx.doi.org/10.1021/ic402683j | Inorg. Chem. 2014, 53, 2910−2921

Table 1. Crystal Parameters and Refinement Data of $M_2[n\mathrm{Ru}]$

	Mg_2[4Ru]	Mg_2[5Ru]	Sr_2[4Ru]	Sr_2[5Ru]	Cd_2[5Ru]
T/K	150(1)	150(1)	150(1)	150(1)	100(1)
formula	$C_{36}H_{18}Mg_2N_6\ O_{12}Ru{\cdot}12H_2O$	$C_{36}H_{18}Mg_2N_6\ O_{12}Ru{\cdot}15H_2O$	$C_{36}H_{18}N_6O_{12}\ RuSr_2{\cdot}9H_2O$	$C_{36}H_{18}N_6O_{12}\ RuSr_2{\cdot}13H_2O$	$C_{36}H_{18}Cd_2N_6\ O_{12}Ru{\cdot}12H_2O$
fw	1068.24	1116.24	1165.02	1237.08	1268.64
cryst syst	trigonal	triclinic	monoclinic	triclinic	monoclinic
space group	$R32$	$P\bar{1}$	$P2_1/c$	$P\bar{1}$	$P2_1/c$
a/Å	14.190(4)	12.6003(8)	24.750(5)	12.397(7)	12.085(3)
b/Å	14.190(4)	14.5810(10)	15.008(3)	13.890(8)	19.169(5)
c/Å	40.593(10)	14.8558(10)	25.792(6)	14.987(9)	24.119(6)
α/deg	90	101.241(2)	90	82.63(2)	90
β/deg	90	96.253(2)	111.957(2)	80.55(2)	90.341(4)
γ/deg	120	108.479(3)	90	72.00(2)	90
V/Å^3	7079(3)	2495.9(3)	8885(3)	2413(3)	5587(3)
Z	6	2	8	2	4
D_{calcd}/g·cm^{-3}	1.503	1.485	1.742	1.703	1.508
reflns collected	41073	15152	140118	40533	83030
unique reflns	5000	10724	28154	12333	18655
GOF	1.131	1.029	1.022	1.076	1.096
R_{int}	0.0435	0.0123	0.0593	0.1722	0.0344
$R\ [I > 2.00\sigma(I)]$	0.0509	0.0665	0.0767	0.0938	0.0898
$R_w{}^a$	0.1661	0.1987	0.2436	0.2791	0.2557

$^a R_w = [\sum(w(F_o{}^2 - F_c{}^2)^2)/\sum w(F_o{}^2)^2]^{1/2}$.

dx.doi.org/10.1021/ic402683j | Inorg. Chem. 2014, 53, 2910−2921

Table 2. Coordination Environment of M^{2+} Ions and Data of Porous Frameworks of $M_2[n\mathbf{Ru}]$

	Mg_2[4Ru]		Mg_2[5Ru]		Sr_2[4Ru]				Sr_2[5Ru]		Cd_2[5Ru]	
	Mg1	Mg2	Mg1	Mg2	Sr1	Sr2	Sr3	Sr4	Sr1	Sr2	Cd1	Cd2
coordination no. of M^{2+}	6	6	6	6	9	7	7	8	7	8	8	5(6)[b]
no. of water molecules coordinated to M^{2+}	3	6	5	4	3	1	2	5	3	7	0	2
void fraction (%)	11.4		24.3		15.0				17.9		43.9	
void space in one unit cell[a] (Å^3)	809		607		1332				431		2451	
pore size (Å)	4.2 × 3.7		3.4 × 5.2		4.0 × 4.0				2.6 × 2.3		12.3 × 6.7	

[a]Calculated by *Platon SQUEEZE*.[24] Noncoordinated water molecules are excluded from the calculations. [b]This cadmium was disordered at two sites.

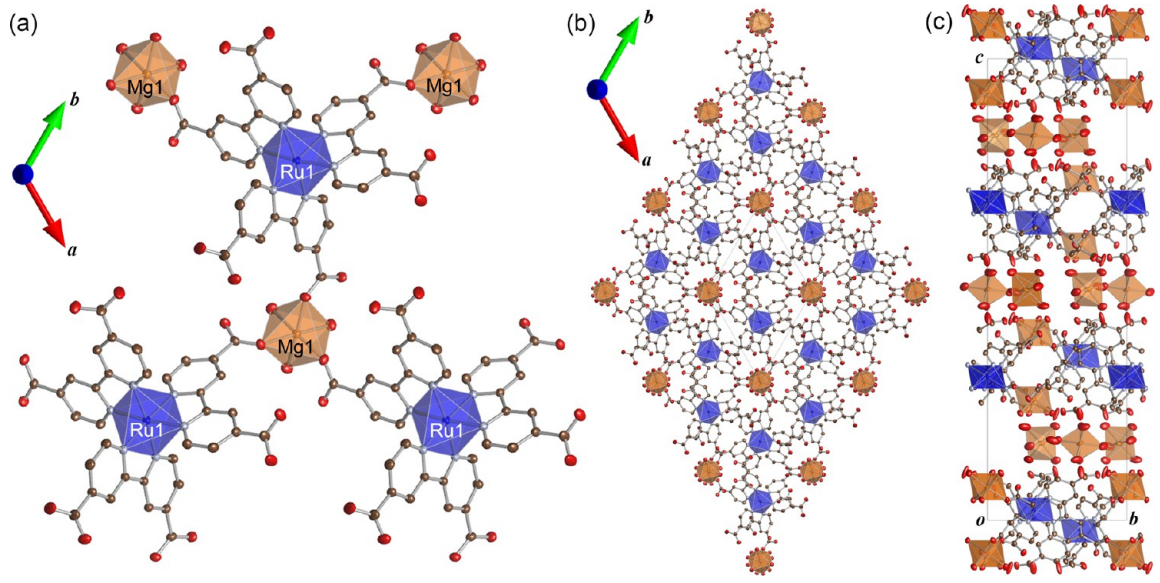

Figure 1. (a) Coordination structures of Mg^{2+} and Ru^{2+} cations, (b) 2D layer structure of $\{[Mg(H_2O)_3][4Ru]\}^{2-}$ in the *ab* plane, and (c) stacking structure viewed along the *a* axis of $\mathbf{Mg_2[4Ru]\cdot 13H_2O}$. The coordination spheres of Ru^{II} and Mg^{II} ions are shown as blue and orange octahedra, respectively. Brown, light blue, and red ellipsoids represent C, N, and O atoms, respectively. Noncoordinated water molecules and H atoms are omitted for clarity.

spectrophotometer. The diffuse-reflectance spectrum of each complex was recorded on the same spectrophotometer equipped with an integrating sphere apparatus. The obtained reflectance spectra were converted to absorption spectra using the Kubelka–Munk function $F(R_\infty)$. Emission and excitation spectra were recorded under various conditions on a Jasco FP-6600 spectrofluorometer. The sample temperature was controlled by a Jasco ETC-273 Peltier-type temperature controller. About 1 mg of the sample was placed between two nonluminescent quartz plates. The typical slit widths of excitation and emission light were 5 and 6 nm, respectively. The emission lifetimes of all of the samples in the solid state were recorded using a Hamamatsu C4780 ps fluorescence lifetime measurement system equipped with a nitrogen laser light source (λ = 337.1 nm). The luminescence quantum efficiency was recorded on a Hamamatsu C9920-02 absolute photoluminescence quantum yield measurement system equipped with an integrating sphere apparatus and a 150-W continuous-wave xenon light source.

Single-Crystal X-ray Structural Determination. Single-crystal X-ray diffraction measurements for $\mathbf{Mg_2[4Ru]\cdot 13H_2O}$, $(\mathbf{Sr_2[4Ru]\cdot 9H_2O})_2$, and $\mathbf{Cd_2[5Ru]\cdot 12H_2O}$ were performed using a Rigaku Mercury CCD diffractometer at the NW2A beamline [λ = 0.6890(1) Å] of the Advanced Ring, Photon Factory, KEK, Japan. The measurements for $\mathbf{Mg_2[5Ru]\cdot 19H_2O}$ and $\mathbf{Sr_2[5Ru]\cdot 14H_2O}$ were performed using the same type of diffractometer with a graphite-monochromated Mo Kα radiation (λ = 0.71069 Å) and a rotating-anode generator. Each single crystal was mounted on a MicroMount with paraffin oil. A nitrogen-gas-flow temperature controller was used to cool the sample. The diffraction data were collected and processed using *CrystalClear*.[19] The structure was solved by direct methods using *SIR2004*[20] and refined by full-matrix least squares using *SHELXL-97*.[21] The non-H atoms were refined anisotropically, while H atoms were refined using the riding model. All calculations were performed using the *Crystal Structure* crystallographic software package.[22] The obtained crystallographic data for each complex are summarized in Table 1. Selected bond lengths around the [*n*Ru] metalloligand are listed in Table S1 (Supporting Information, SI). The coordination environment of the M^{2+} ion and the data about the porosity of each $\mathbf{M_2}[n\mathbf{Ru}]$ are summarized in Table 2. Estimation of the void volume in each complex was calculated by *Platon SQUEEZE*,[23] wherein the non-coordinated water molecules were excluded (but coordinated water molecules were included) in the calculation.

Powder X-ray Diffraction (PXRD). PXRD measurements were carried out using a Rigaku SPD diffractometer at beamline BL-8B of the Photon Factory, KEK, Japan. The wavelength of the synchrotron X-ray was 0.9985(1) Å. The sample was placed in a glass capillary of 0.5 mm diameter. The relative humidity (RH) inside each capillary was controlled by using saturated salt solutions (LiCl, KCH_3COO, K_2CO_3, NaCl, and KCl for RH = 11, 23, 43, 75, and 85%, respectively)[24] as the water-vapor source.

Adsorption Isotherms. The adsorption isotherms for water and methanol vapors at 298 K were performed using an automatic volumetric adsorption apparatus (BELSORP-MAX; BEL Japan, Inc.)

Thermogravimetric Analysis (TGA). TGA and differential thermal analysis were performed using a Rigaku ThermoEvo TG8120 analyzer.

RESULTS AND DISCUSSION

Crystal Structures of [4Ru]-Based PCPs. To design a wide variety of porous frameworks, we used two isomeric

dx.doi.org/10.1021/ic402683j | Inorg. Chem. 2014, 53, 2910–2921

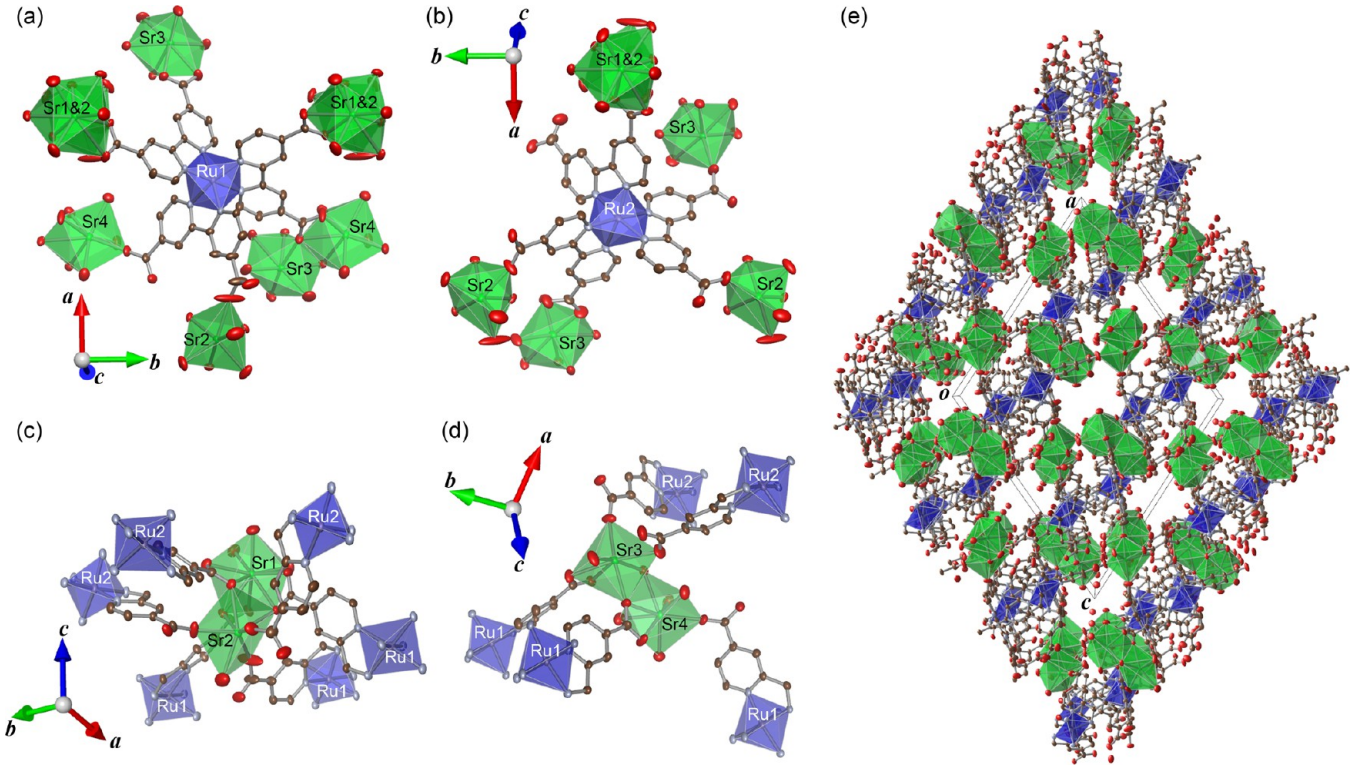

Figure 2. Coordination environments of (a and b) two crystallographically independent [**4Ru**] and (c and d) four Sr^{2+} cations. (e) Packing diagram of $(\mathbf{Sr_2}[\mathbf{4Ru}]\cdot\mathbf{9H_2O})_2$ viewed along the *b* axis. The coordination spheres of the Ru^{II} and Sr^{II} ions are shown as blue and green octahedra, respectively. Brown, light-blue, and red ellipsoids represent C, N, and O atoms, respectively. Noncoordinated water molecules and H atoms are omitted for clarity.

ruthenium(II) metalloligands, [**4Ru**] and [**5Ru**]. The different positions of the carboxyl groups in the dcbpy ligand should play an important role in the design of the porous framework. In this section, we discuss two PCPs fabricated from the [**4Ru**] metalloligand, bearing six carboxyl groups, with each group positioned at the top of the coordination octahedron of the Ru^{II} center. Figure 1a shows the coordination environment of the Mg^{2+} cation and the [**4Ru**] metalloligand of $\mathbf{Mg_2}[\mathbf{4Ru}]\cdot\mathbf{13H_2O}$. This complex crystallized in the trigonal *R*32 space group and one Ru^{II} cation, two Mg^{II} cations, and one 4,4′-dcbpy ligand were found to be crystallographically independent. Because the Ru1 atom was found to be on the 3-fold helix axis, three 4,4′-dcbpy ligands in one [**4Ru**] anion are equivalent to each other. The observed Ru−N bond lengths [2.057(3) and 2.057(4) Å] are almost similar to the starting metalloligand [**4Ru**] (2.046−2.068 Å),[17] indicating that the Ru cation remains in the divalent oxidation state. Interestingly, only one enantiomer, Δ-[Ru(4,4′-dcbpy)$_3$]$^{4-}$, was found in this crystal structure, consistent with the acentric space group (*R*32). The observed C−O bond distances ranging between 1.244(5) and 1.261(6) Å suggest that all of the carboxyl groups are deprotonated and three of the six are bonded to Mg^{II} cations in the monodentate mode, as shown in Figure 1a. Two types of Mg^{II} cations with six-coordinated octahedral structure were found. One type, located on the 3-fold helical axis, is bound by three carboxyl groups and three water molecules (which occupied the *fac* positions) to form two-dimensional (2D) honeycomb-like coordination networks, $\{[Mg(H_2O)_3[4Ru]\}_n^{2n-}$, in the *ab* plane, as shown in Figure 1b. As a result, the uncoordinated carboxylates of [**4Ru**] are exposed on both surfaces of the 2D coordination sheet. The other six-coordinated octahedral structure of the Mg^{2+} cation is surrounded by six-coordinated water molecules and located between two 2D coordination sheets of $\{[Mg(H_2O)_3[4Ru]\}_n^{2n-}$, as shown in Figure 1c. A void space of ∼809 Å^3 (11.4% void fraction), as calculated by *Platon SQUEEZE*,[24] was found in the $[Mg(H_2O)_6]^{2+}$ layer. Considering the results of elemental analysis and the water vapor adsorption isotherm (Figure 7), this void space is probably occupied by more than four water molecules per [**4Ru**] metalloligand.

We used several different metal ions in the syntheses of [***n*Ru**]-based PCPs to control not only the porous structure but also the structural flexibility. Parts a and b of Figure 2 show the coordination modes of two independent [**4Ru**] in $(\mathbf{Sr_2}[\mathbf{4Ru}]\cdot\mathbf{9H_2O})_2$. This complex crystallized in the monoclinic $P2_1/c$ space group, and two crystallographically independent [**4Ru**] metalloligands and four Sr^{2+} cations were found in one unit cell. Similar to $\mathbf{Mg_2}[\mathbf{4Ru}]\cdot\mathbf{13H_2O}$, the observed Ru−N bond distances [2.043(4)−2.082(4) Å] suggest that the oxidation state of the Ru centers remains in the divalent state. In contrast to the chiral crystal of $\mathbf{Mg_2}[\mathbf{4Ru}]\cdot\mathbf{13H_2O}$, $(\mathbf{Sr_2}[\mathbf{4Ru}]\cdot\mathbf{9H_2O})_2$ formed a racemic crystal composed of the Λ and Δ isomers of [**4Ru**]. As shown in Figure 2a, one [**4Ru**] metalloligand (labeled as Ru1) was bonded to nine Sr^{2+} cations. The observed C−O bond lengths for all of the carboxyl groups were in the range of 1.235(12)−1.278(6) Å, suggesting that all of the carboxyl groups of [**4Ru**] were deprotonated.[17] Three of the six carboxyl groups were not only bonded in the bidentate mode but also bridged between two Sr^{2+} cations. Two of the remaining carboxyl groups were bonded to Sr^{2+} cations in simple monodentate mode and one carboxyl group was bonded to Sr^{2+} cation in the bidentate mode. In contrast, another

dx.doi.org/10.1021/ic402683j | *Inorg. Chem.* 2014, 53, 2910−2921

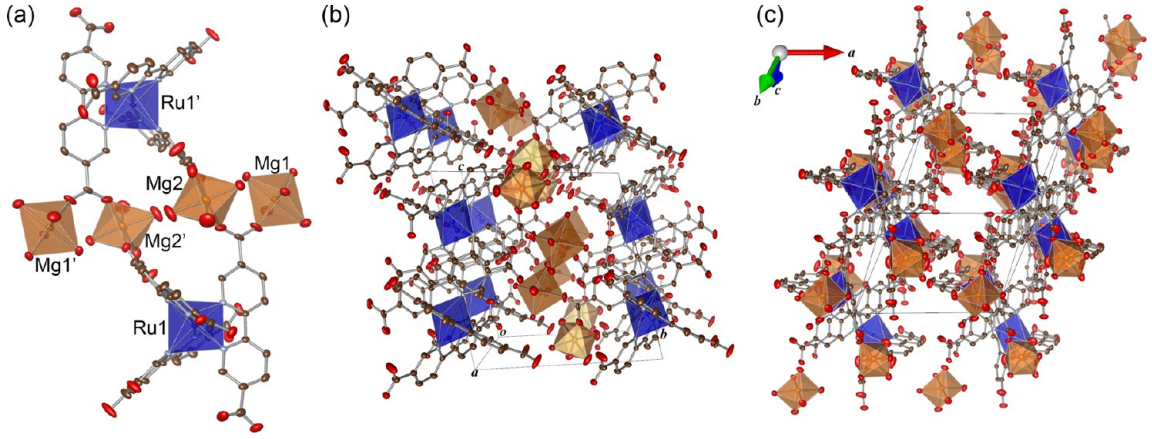

Figure 3. (a) Dimerized structure and (b and c) crystal packing viewed along the *a* and *c*−*b* axes of $\mathbf{Mg_2[5Ru]\cdot 19H_2O}$, respectively. The coordination spheres of the Ru^{II} and Mg^{II} ions are shown as blue and orange octahedra, respectively. Brown, light-blue, and red ellipsoids represent C, N, and O atoms, respectively. Noncoordinated water molecules and H atoms are omitted for clarity.

crystallographically independent [**4Ru**] metalloligand (labeled as Ru2) was surrounded by only six Sr^{2+} cations, as shown in Figure 2b. All C−O bond lengths [1.227(8)−1.284(9) Å] also indicate that all six carboxyl groups were in the deprotonated form. Interestingly, one of the six carboxyl groups was not coordinated to any cations. Four of the carboxylate groups were coordinated in a simple monodentate fashion, and only one carboxyl group was bonded in a bidentate fashion, in which one O atom was bridged between two Sr^{2+} cations. Parts c and d of Figure 2 show the coordination environments of four crystallographically independent Sr^{2+} cations. Sr1 and Sr2 were bridged by three O atoms of the carboxyl groups from three different [**4Ru**] metalloligands, which were also coordinated to Sr1 in a bidentate fashion. Three water molecules were also bonded to Sr1, resulting in the nine-coordinated polyhedral structure. In contrast, only one water molecule was bonded to Sr2, together with three monodentate carboxyl groups of [**4Ru**], to form a seven-coordinated structure. As a result, this dinuclear Sr core was coordinated by six [**4Ru**] metalloligands. The other two Sr^{2+} cations, Sr3 and Sr4, also formed a dinuclear core bridged by one water molecule and one O atom from the carboxyl group of [**4Ru**]. This bridging carboxyl group also coordinated to Sr4 in a bidentate fashion. In addition to the bridging water molecule, four water molecules and one monodentate carboxyl group were bonded to Sr4 to form an eight-coordinated polyhedral structure. In contrast, only one terminal water molecule and two bidentate and one monodentate carboxyl groups coordinated to Sr3 to form a seven-coordinated structure. Because of the coordination polymerization of the [**4Ru**] metalloligand by the Sr^{2+} cations, a three-dimensional (3D) coordination network structure was formed, as shown in Figure 2e. Notably, small one-dimensional (1D) void spaces with ∼4.0 Å diameter along the *b* axis were found at the center, corners of the *ac* plane, and midpoints of the *a* and *c* axes. Several noncoordinated crystal water molecules were found in these voids by X-ray analysis. The estimated void volume excluding noncoordinated crystal water molecules was 1332 $Å^3$ (15.0% void fraction) in one unit cell.

As discussed above, there are large differences in the crystal structures between $\mathbf{Mg_2[4Ru]\cdot 13H_2O}$ and $(\mathbf{Sr_2[4Ru]\cdot 9H_2O})_2$, even though both use the same metalloligand [**4Ru**]. This metalloligand forms a 2D coordination sheet structure by the reaction with the Mg^{2+} cation, while the reaction with the Sr^{2+} cation leads to the formation of a 3D network structure. These differences are probably due to the large differences in the hydration enthalpy and ionic radius between the two cations. In fact, the Mg^{2+} cations in $\mathbf{Mg_2[4Ru]\cdot 13H_2O}$ were coordinated by three or six water molecules, whereas the Sr^{2+} cations in $(\mathbf{Sr_2[4Ru]\cdot 9H_2O})_2$ are surrounded by at most three coordinated water molecules. It should be noted that both PCPs have large amounts of coordinated and noncoordinated water molecules accompanied by small void spaces with a void fraction of 11.4% for $\mathbf{Mg_2[4Ru]\cdot 13H_2O}$ and 15.0% for $(\mathbf{Sr_2[4Ru]\cdot 9H_2O})_2$. These void spaces and fractions suggest that both compounds can have vapor adsorption abilities.

Crystal Structures of [5Ru]-Based PCPs. Because the ruthenium(II) metalloligand [**5Ru**] is one of the geometrical isomers of [**4Ru**], its six carboxyl groups are at different positions from those of [**4Ru**]. Considering the difference in the molecular structures of these [***n*Ru**], the [**5Ru**] metalloligand may act as a quasi-1D pillar ligand, while [**4Ru**] acts as a 3D connecting ligand. From this point of view, we investigated the syntheses of porous frameworks fabricated on the [**5Ru**] metalloligand. Figure 3a shows the coordination environments of Ru^{2+} and Mg^{2+} cations of $\mathbf{Mg_2[5Ru]\cdot 19H_2O}$. This complex crystallized in the triclinic $P\bar{1}$ space group. Only one Ru^{2+}, two Mg^{2+} cations, and three dcbpy ligands were found to be crystallographically independent. Moreover, the observed Ru−N bond distances [2.053(3)−2.068(3) Å] indicate that the oxidation state of the Ru^{II} center was not changed in the reaction with the magnesium salt. Interestingly, the two enantiomers, Λ- and Δ-[**5Ru**], were connected by two Mg^{2+} cations, as shown in Figure 3a. The observed C−O bond lengths [1.225(6)−1.266(5) Å] suggests that all of the carboxyl groups were deprotonated to form the $[\mathbf{5Ru}]^{4-}$ anion. Only two of the six carboxyl groups of the [**5Ru**] metalloligand coordinate to the different Mg1, Mg2, and Mg2′ cations. One carboxyl group is coordinated to Mg2′ in a monodentate fashion. The other carboxyl group is bridged between the Mg1 and Mg2 cations. These Mg^{2+} cations have a six-coordinated octahedral geometry, as is commonly observed. The coordination site of Mg1 is occupied by one carboxyl O atom and five water molecules. Mg2 is coordinated by four water molecules and two carboxyl O atoms at the cis position to form the Mg^{2+}-bridged dimerized structure $\{[Mg(H_2O)_5]_2[Mg(H_2O)_4]_2[5Ru]_2\}$. As a result, no coordination-polymer structure was formed in this complex, which is in contrast to

dx.doi.org/10.1021/ic402683j | Inorg. Chem. 2014, 53, 2910−2921

the [**4Ru**]-based PCP, **Mg_2[4Ru]·13H_2O**. Along the *b* axis, an alternately stacked structure fabricated from the $[Mg(H_2O)_n]^{2+}$ cations and $[\mathbf{5Ru}]^{4-}$ anions formed, as shown in Figure 3b. In spite of the lack of a coordination-polymer structure, small void space was found along the *c*−*b* axis, as shown in Figure 3c, and the void fraction in one unit cell was estimated to be 24.3% (607 $Å^3$) by *Platon SQUEEZE*. As expected from the result of elemental analysis, six crystal (noncoordinated) water molecules were found in this crystal structure. Four were hydrogen-bonded to the O atom of the noncoordinated carboxyl groups and/or water molecules bound at the Mg^{2+} cation.

Figure 4a shows the coordination environment of the [**5Ru**] metalloligand in the **Sr_2[5Ru]·14H_2O** complex. This complex

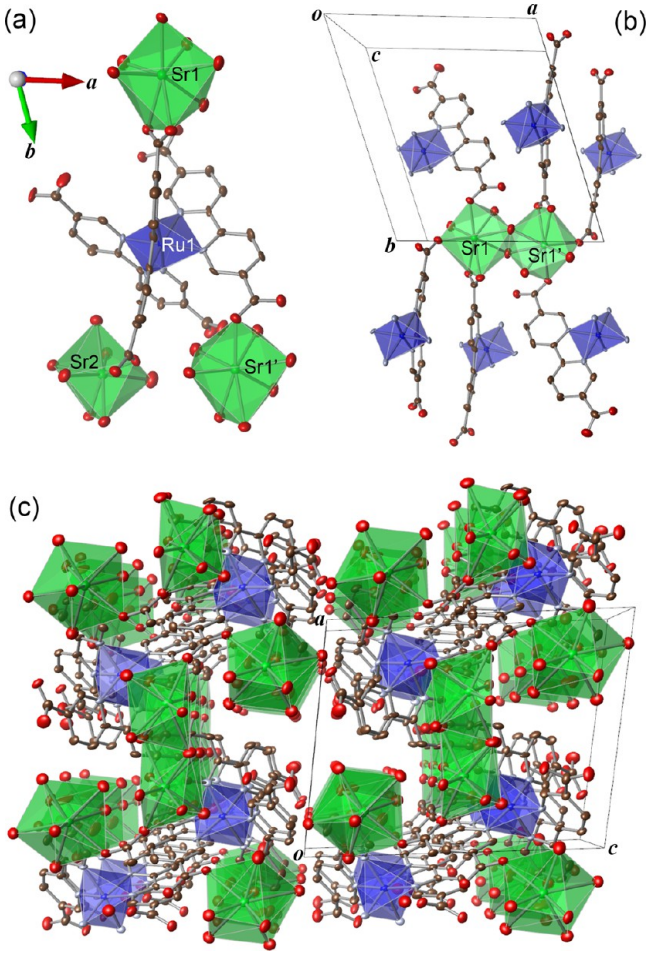

Figure 4. Coordination environments of (a) [**5Ru**] and (b) Sr1 cation. (c) Packing diagram of **Sr_2[5Ru]·14H_2O** viewed along the *b* axis. The coordination spheres of the Ru^{II} and Sr^{II} ions are shown as blue and green octahedra, respectively. Brown, light-blue, and red ellipsoids represent C, N, and O atoms, respectively. Noncoordinated water molecules and H atoms are omitted for clarity.

crystallized in the triclinic $P\bar{1}$ space group. In the unit cell, one Ru^{2+} cation, two Sr^{2+} cations, and three dcbpy ligands were found to be crystallographically independent. The observed Ru−N bond distances were in the range of the typical Ru^{II}−N distance [2.044(7)−2.077(7) Å], indicating the divalent oxidation state, similar to that of the other [***n*Ru**]-based PCPs. The observed C−O bond distances were also in the range of the typical deprotonated carboxylate form. One of the three dcbpy ligands was found to coordinate to two different Sr^{2+} cations, Sr1 and Sr2, by carboxyl groups. The second was bonded to one Sr^{2+} cation in a monodentate fashion. The final dcbpy ligand did not coordinate to any metal cations. The coordination sites of Sr1 were occupied by four carboxyl O atoms and three water molecules to form a seven-coordinated polyhedral structure, as shown in Figure 4b. Two of the three water molecules were bridged between two Sr1 cations, containing the crystallographic inversion center at the midpoint. In contrast, the other Sr^{2+} cation, Sr2, was coordinated by only one carboxyl O atom and seven water molecules, as shown in Figure 4a. In other words, the Sr2 cation did not act as the bridging metal ions between the two [**5Ru**] metalloligands; instead, it acted as the terminal end of the coordination polymer fabricated from [**5Ru**] and the Sr1 cations. This configuration resulted in the formation of a 2D coordination sheet structure, as shown in Figure 4c (please note that there is no coordination bond crossing the *ab* plane). Similar to the other [***n*Ru**]-based PCPs, a small void space was found along the *b* axis between the 2D coordination sheets. The diameter of this 1D pore was estimated to be less than 3 Å.

Parts a−c of Figure 5 show the crystal structure of **Cd_2[5Ru]·12H_2O**. This complex crystallized in the monoclinic $P2_1/c$ space group. There were one crystallographically independent Ru^{2+} cation, two Cd^{2+} cations, and three dcbpy ligands in the unit cell. The enantiomers, Λ- and Δ-[**5Ru**], formed one racemic crystal by the coordination polymerization reaction with the Cd^{2+} cation. Similar to the other [***n*Ru**]-based PCPs, the observed Ru−N bond distances [2.056(6)−2.082(5) Å] indicated that the Ru center remained in the divalent oxidation state. The observed C−O bond distances also suggest that all of the carboxyl groups of [**5Ru**] were deprotonated. In contrast to the other [**5Ru**]-based complexes, all carboxyl groups were found to coordinate to the Cd^{2+} cations, as shown in Figure 5a. One of the six carboxyl groups was bonded in the monodentate mode, while four carboxyl groups were coordinated in a bidentate mode. The final carboxyl group not only was bonded in the bidentate mode but also was bridged between two Cd^{2+} cations. Figure 5b shows the coordination environment of two crystallographically independent Cd^{2+} cations. Cd1 formed an eight-coordinated polyhedral structure with four sets of bidentate carboxylates from [**5Ru**]. In contrast, Cd2 was found to be disordered at two positions. However, both sites were trigonal-bipyramidal. The three coordination sites of Cd2 in the basal plane were occupied by two water molecules and one carboxylate in a monodentate fashion. The two axial positions were occupied by one bridging carboxylate and one carboxylate with either monodentate or bidentate binding, resulting in disorder of the Cd2 cation at the two sites. Interestingly, a relatively large 1D void space was formed along the *a* axis, as shown in Figure 5c. The pore size of this 1D channel and void volume in one unit cell were estimated to be 12.3 × 6.7 Å and 2451 $Å^3$, significantly larger than those of the other [***n*Ru**]-based PCPs.

As described above, we have succeeded in the syntheses of three different PCPs by coordination polymerization between the [**5Ru**] metalloligand with Mg^{2+}, Sr^{2+}, and Cd^{2+} metal ions. In these reactions, the oxidation state of the Ru center commonly remains in the divalent state, and all six carboxyl groups are deprotonated. As expected from the structural difference between the two isomeric ruthenium(II) metalloligands, [**4Ru**] and [**5Ru**], the crystal structures of [**5Ru**]-based PCPs are largely different from the structures of [**4Ru**]-based PCPs. The layer-by-layer structure fabricated from the

dx.doi.org/10.1021/ic402683j | *Inorg. Chem.* 2014, 53, 2910−2921

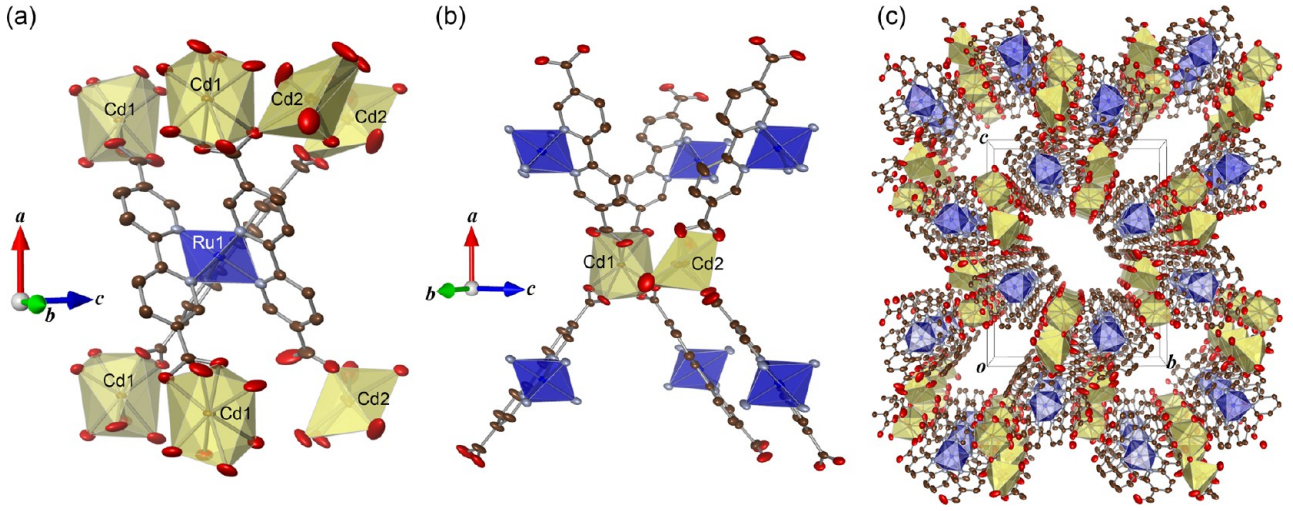

Figure 5. Coordination environments of (a) [**5Ru**] and (b) Cd^{2+} cations. (c) Packing diagram of $\mathbf{Cd_2}$[**5Ru**]·$\mathbf{12H_2O}$ viewed along the *a* axis. The coordination spheres of the Ru^{II} and Cd^{II} ions are shown as blue and yellow octahedra, respectively. Brown, light-blue, and red ellipsoids represent C, N, and O atoms, respectively. Noncoordinated water molecules and H atoms are omitted for clarity.

alternative stacks of M^{2+} cation and [**5Ru**] anion was formed in the $\mathbf{M_2}$[**5Ru**] system (along the *b* axis in both $\mathbf{Mg_2}$[**5Ru**]·$\mathbf{13H_2O}$ and $\mathbf{Sr_2}$[**5Ru**]·$\mathbf{14H_2O}$ and along the *a* axis in $\mathbf{Cd_2}$[**5Ru**]·$\mathbf{12H_2O}$). One of the remarkable structural features in the $\mathbf{M_2}$[**5Ru**] system is the large 1D porous structure formed in the $\mathbf{Cd_2}$[**5Ru**]·$\mathbf{12H_2O}$ complex. Considering the fact that fewer water molecules coordinated to the Cd^{2+} cations than in the other $\mathbf{M_2}$[**5Ru**] (Table 2), the softness of the Lewis acidity of the metal ion plays an important role in the construction of a porous framework with a large pore size.

Vapor-Induced Structural Transformations. As discussed in the Introduction, we previously reported that reversible amorphous−crystalline phase transitions of the cobalt(III) metalloligand based PCPs, {Ln[Co(4,4′-dcbpy)$_3$]}, were induced by vapor adsorption/desorption.[16] Because we have used the ruthenium(II) metalloligands [**4Ru**], which has almost the same molecular structure as that of [Co(4,4′-dcbpy)$_3$]$^{3-}$, similar vapor-induced structural transformations are expected. In order to clarify the structural flexibility of the newly obtained PCPs $\mathbf{M_2}$[***n*Ru**], we measured the PXRD patterns under several conditions. Figure 6 shows the changes in the PXRD patterns of $\mathbf{Mg_2}$[**4Ru**] and $\mathbf{Sr_2}$[**4Ru**]. The synthesized samples showed diffraction patterns very similar to the simulated PXRD pattern calculated from their crystal structures, indicating that their porous frameworks are stable enough to retain their structures in air. After drying at 423 K for 1 day, the patterns of both $\mathbf{M_2}$[**4Ru**] changed remarkably, suggesting that the porous structures could not be retained without crystal water molecules. In TGA, ∼21.6% and 15.2% weight losses were observed at 423 K for $\mathbf{Mg_2}$[**4Ru**] and $\mathbf{Sr_2}$[**4Ru**], respectively, which agreed with the calculated amount of hydrated water molecules (21.1% and 14.0% for $\mathbf{Mg_2}$[**4Ru**]·$\mathbf{13H_2O}$ and $\mathbf{Sr_2}$[**4Ru**]·$\mathbf{9H_2O}$, respectively). This result suggests that most of the crystal water molecules included in $\mathbf{M_2}$[**4Ru**] were removed at 423 K (Figure S1 in the SI). In fact, negligible weight losses were observed for the dried $\mathbf{M_2}$[**4Ru**], and temperature dependences of IR spectra of $\mathbf{Mg_2}$[**4Ru**]·$\mathbf{13H_2O}$ and $\mathbf{Sr_2}$[**4Ru**]·$\mathbf{9H_2O}$ clearly showed that the ν(O−H) absorption band remarkably decreased above 423 K (Figure S2 in the SI). After these dried samples were exposed to saturated water vapor, the observed patterns were almost

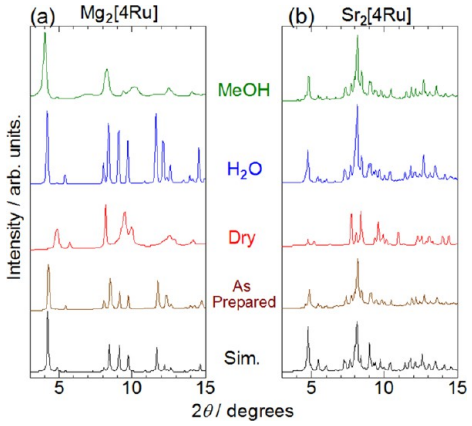

Figure 6. Changes of the PXRD patterns [λ = 0.9985(1) Å] of (a) $\mathbf{Mg_2}$[**4Ru**] and (b) $\mathbf{Sr_2}$[**4Ru**] under exposure to dried air, H_2O, and MeOH vapor at room temperature. The bottom two are the patterns of as-prepared samples and simulated patterns calculated from corresponding crystal structures.

identical with the simulated patterns, indicating that both $\mathbf{M_2}$[**4Ru**] can reversibly adsorb/desorb water vapor, accompanied by structural transformation. Interestingly, the diffraction patterns of dried $\mathbf{Mg_2}$[**4Ru**] and $\mathbf{Sr_2}$[**4Ru**] also changed remarkably under exposure to methanol vapor, suggesting the possibility of methanol vapor adsorption. It should be noted that the pattern of $\mathbf{Sr_2}$[**4Ru**] under exposure to methanol vapor is almost the same as that under water-vapor exposure, whereas the patterns of $\mathbf{Mg_2}$[**4Ru**] under methanol and water vapor were different from each other. Thus, the methanol-adsorbed structure of $\mathbf{Sr_2}$[**4Ru**] should almost be the same porous framework structure of ($\mathbf{Sr_2}$[**4Ru**]·$\mathbf{9H_2O}$)$_2$, while the methanol- and water-adsorbed structures of $\mathbf{Mg_2}$[**4Ru**] should be different. We also analyzed the changes in the PXRD patterns of $\mathbf{M_2}$[**5Ru**] and found that the porous frameworks of $\mathbf{Mg_2}$[**5Ru**] collapsed irreversibly by drying of the compound. The framework of $\mathbf{Cd_2}$[**5Ru**], with the largest pore size, was unstable even in air (Figure S3 in the SI).

In order to clarify the vapor adsorption properties of $\mathbf{M_2}$[**4Ru**], water and methanol vapor adsorption isotherms were measured. Figure 7 shows the water vapor adsorption

dx.doi.org/10.1021/ic402683j | Inorg. Chem. 2014, 53, 2910−2921

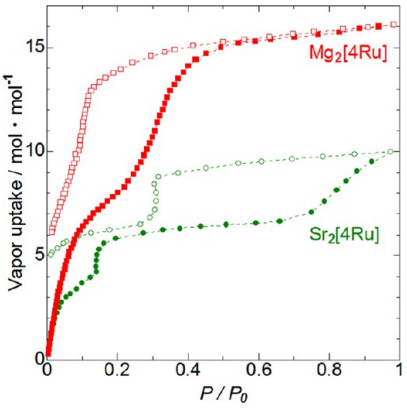

Figure 7. Water vapor adsorption isotherms of **Mg$_2$[4Ru]** (red squares) and **Sr$_2$[4Ru]** (green circles) at 298 K. Closed and open symbols show adsorption and desorption processes, respectively.

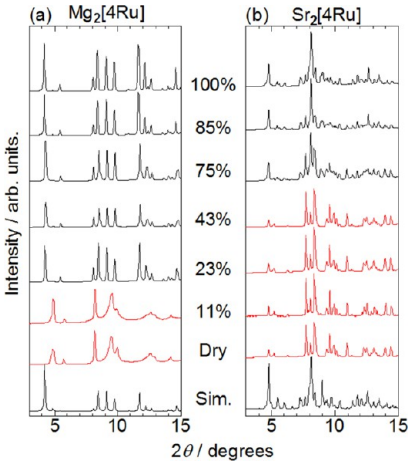

Figure 8. PXRD patterns [λ = 0.9985(1) Å] of the RH dependence of (a) **Mg$_2$[4Ru]** and (b) **Sr$_2$[4Ru]** at room temperature. Bottom patterns are simulated patterns calculated from corresponding crystal structures.

isotherms of **Mg$_2$[4Ru]** and **Sr$_2$[4Ru]** at 298 K. Before each measurement, the samples were dried at 373 K under vacuum to remove all hydrated water. As expected from the crystal structures with large hydration numbers, both PCPs can adsorb large amounts of water vapor, over 10 mol mol^{-1} per **[4Ru]** unit. It should be noted that the adsorption profile of **Sr$_2$[4Ru]** was remarkably different from that of **Mg$_2$[4Ru]**. The water vapor adsorption of **Sr$_2$[4Ru]** proceeded in three steps: after two-step adsorption at low pressure (below P/P_0 = 0.20, ca. 5.8 mol mol^{-1}), the isotherm reached a wide plateau region, after which it showed a sudden increase above P/P_0 = 0.75. The saturation point was 10 mol mol^{-1}, which is very close to the hydration number of **Sr$_2$[4Ru]**. During the desorption process, the absorbed amount was almost constant above P/P_0 = 0.32, after which it sharply decreased to ~6 mol mol^{-1}, which is almost consistent with the number of coordinated water molecules in **Sr$_2$[4Ru]**. In contrast, the isotherm for **Mg$_2$[4Ru]** showed a two-step adsorption profile below P/P_0 = 0.5 via a small shoulder at P/P_0 = 0.20. The saturated amount was 16.0 mol mol^{-1}, which is larger than that of **Sr$_2$[4Ru]** and is close to the hydration number for **Mg$_2$[4Ru]** as estimated from elemental analysis. In the desorption process, the absorbed amount decreased sharply below P/P_0 = 0.15. These large hysteresis values for both **Sr$_2$[4Ru]** and **Mg$_2$[4Ru]** suggest that structural transition occurs during the vapor adsorption and desorption processes. In order to gain more information about the water-vapor-induced structural transition, the PXRD patterns of the RH dependences of **Sr$_2$[4Ru]** and **Mg$_2$[4Ru]** were measured. As shown in Figure 8, the PXRD pattern of **Mg$_2$[4Ru]** interestingly changed to almost the same pattern as the simulated pattern above RH = 23%, where the amount of water vapor adsorbed was about 8.6 mol mol^{-1}. Considering the fact that the number of water molecules coordinated to the Mg^{2+} cations in **Mg$_2$[4Ru]** was determined to be 9 mol per **[4Ru]** unit (Table 2), the driving force for regeneration of the porous 2D sheet structure should be the adsorption and coordination of water molecules to two different Mg^{2+} cations. The second adsorption of water vapor above P/P_0 = 0.2 corresponds to adsorption to the porous channels formed in the $[Mg(H_2O)_6]^{2+}$ cationic layers. In contrast, the pattern of **Sr$_2$[4Ru]** was still unchanged at this low-RH region, where about 5 mol mol^{-1} of water vapor was adsorbed. A pattern almost identical with the simulated pattern of **Sr$_2$[4Ru]** was observed above RH = 75%, which corresponds to the third adsorption step observed in the water vapor adsorption isotherm. As discussed in the crystal structure section, the number of water molecules coordinated to Sr^{2+} cations per **[4Ru]** unit is estimated to be 5, suggesting that the two-step increases observed in the adsorption isotherm should correspond to the adsorption and coordination of water to the Sr^{2+} cations. However, in contrast to **Mg$_2$[4Ru]**, a larger amount of water adsorption is required to regenerate the porous framework. This difference may originate from the difference in the hydration enthalpy between Mg^{2+} and Sr^{2+}. The larger hydration enthalpy of Mg^{2+} compared to Sr^{2+} could promote coordination of the adsorbed water molecules in the crystal of **Mg$_2$[4Ru]**, resulting in regeneration of the porous 2D sheet structure at a lower RH region than that of **Sr$_2$[4Ru]**.

Figure 9 shows the methanol vapor adsorption isotherms of **Mg$_2$[4Ru]** and **Sr$_2$[4Ru]** at 298 K. As expected from the

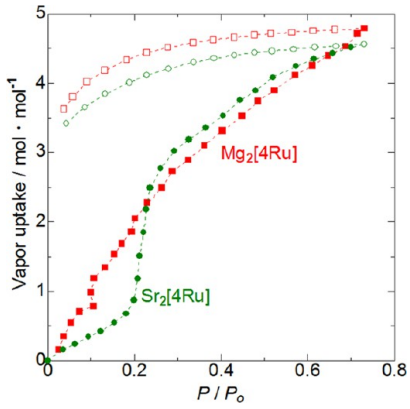

Figure 9. Methanol vapor adsorption isotherms of **Mg$_2$[4Ru]** (red squares) and **Sr$_2$[4Ru]** (green circles) at 298 K. Closed and open symbols show adsorption and desorption processes, respectively.

changes in the PXRD patterns (Figure 6), these two PCPs can adsorb methanol vapor. In contrast to the large difference between the saturated water vapor adsorption amounts of **Mg$_2$[4Ru]** and **Sr$_2$[4Ru]**, the adsorbed methanol amounts at P/P_0 = 0.73 are almost the same: 4.7 and 4.5 mol mol^{-1} per **[4Ru]** unit for **Mg$_2$[4Ru]** and **Sr$_2$[4Ru]**, respectively. As mentioned above, the structure of the methanol-adsorbed **Sr$_2$[4Ru]** was almost the same as that of fully hydrated

dx.doi.org/10.1021/ic402683j | Inorg. Chem. 2014, 53, 2910−2921

$(\mathbf{Sr_2[4Ru]\cdot 9H_2O})_2$, whereas the methanol- and water-adsorbed phases of $\mathbf{Mg_2[4Ru]}$ showed different framework structures (Figure 6). Considering the difference between the molecular volumes of methanol and water, the guest-accessible volume of the $\mathbf{Sr_2[4Ru]}$ complex will be fully occupied by the adsorbed methanol molecules, resulting in the formation of almost the same structure as that of the fully hydrated $(\mathbf{Sr_2[4Ru]\cdot 9H_2O})_2$. In contrast, the saturated amount of methanol vapor adsorption of $\mathbf{Mg_2[4Ru]}$ is quite smaller than the amount of water vapor adsorption, suggesting that the volume occupied by the adsorbed methanol is not sufficient to fully occupy the guest-accessible space in $\mathbf{Mg_2[4Ru]\cdot 16H_2O}$. As a result, the methanol-adsorbed structure of $\mathbf{Mg_2[4Ru]}$ will be different from the structure of $\mathbf{Mg_2[4Ru]\cdot 16H_2O}$.

Before each vapor adsorption measurement, these PCPs were dried at 373 K for 1 day to remove all hydrated water in order to form the anhydrous state of the PCPs. In the anhydrous state, the coordination sites of the M^{2+} cation could either be occupied by the carboxyl groups of the [**4Ru**] metalloligand or remain in a coordinatively unsaturated state. Considering the fact that these unsaturated sites can act as the guest adsorption sites,[6,10] methanol vapor is probably adsorbed and coordinated to the M^{2+} centers. In the case of water vapor adsorption, the first guest adsorption site should also be the same coordinatively unsaturated sites. However, the additional vapor adsorption occurs because of the smaller molecular volume and high hydrogen-bonding ability of water vapor compared to methanol. The isotherm of $\mathbf{Sr_2[4Ru]}$ showed a sharp increase at $P/P_0 = 0.20$, whereas the adsorption amount of $\mathbf{Mg_2[4Ru]}$ monotonically increased from the low-pressure region. This difference can be related to structural dimensionality. In contrast to the 2D coordination sheet structure of $\mathbf{Mg_2[4Ru]\cdot 13H_2O}$, $(\mathbf{Sr_2[4Ru]\cdot 9H_2O})_2$ has a more rigid 3D coordination network structure, supported by the bridging carboxylates, implying that the structural flexibility of $\mathbf{Sr_2[4Ru]}$ is lower than that of $\mathbf{Mg_2[4Ru]}$. In addition, the 2D-layered structure of $\mathbf{Mg_2[4Ru]\cdot 13H_2O}$ may enable the complex to retain the guest-accessible layers formed from the Mg^{2+} cations, even in the anhydrous form. Moreover, these two PCPs were found to hardly adsorb CO_2 gas (less than 0.1 mol mol^{-1}; see Figure S4 in the SI), implying that their porous channels in the dried states would have a highly hydrophilic nature and/or a smaller pore diameter than the molecular size of CO_2.

Absorption and Emission Properties. As mentioned in the Introduction, ruthenium(II) polypyridine complexes show interesting absorption and emission properties derived from metal-to-ligand charge-transfer (MLCT) transitions.[12] To investigate the effect of coordination polymerization on the absorption and emission properties of the metalloligands [***n*Ru**], UV diffuse-reflectance and luminescence spectra in the solid state were measured. The results were compared with those of the metalloligands in a basic aqueous solution and are shown in Figure 10. The observed energies of the absorption edge and emission maxima are summarized in Table 3. The ruthenium(II) metalloligands [**4Ru**] and [**5Ru**] showed absorption bands at 467 and 484 nm and emission bands at 633 and 668 nm, respectively. These absorption and emission bands are assigned as the singlet and triplet MLCT transitions; our results are consistent with the previous report by Kalyanasundaram et al.[12] All of the obtained $\mathbf{M_2[}n\mathbf{Ru]}$ PCPs showed a very broad absorption band below 600 nm and a emission band at ~680 nm. The emission lifetimes for $\mathbf{Mg_2[5Ru]\cdot 19H_2O}$ (48 ns) and $(\mathbf{Sr_2[4Ru]\cdot 9H_2O})_2$ (256 ns)

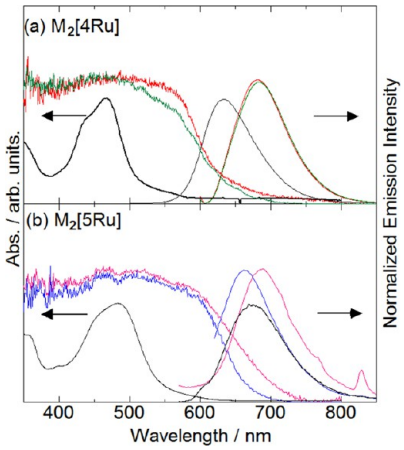

Figure 10. UV diffuse-reflectance and luminescence spectra of (a) $\mathbf{Mg_2[4Ru]\cdot 13H_2O}$ (red line) and $\mathbf{Sr_2[4Ru]\cdot 9H_2O}$ (green), (b) $\mathbf{Mg_2[5Ru]\cdot 19H_2O}$ (blue), and $\mathbf{Cd_2[5Ru]\cdot 12H_2O}$ (purple) from the solid state at room temperature. Spectra of metalloligands [***n*Ru**] in basic aqueous solutions are shown in black.

Table 3. Absorption and Emission Spectral Data of $\mathbf{M_2[}n\mathbf{Ru]}$ at Room Temperature

complex	λ_{abs} (nm)	λ_{em} (nm)
[**4Ru**](aq)	436, 467	633[b]
$\mathbf{Mg_2[4Ru]\cdot 13H_2O}$	600[a]	681[c]
$(\mathbf{Sr_2[4Ru]\cdot 9H_2O})_2$	595[a]	683[c]
[**5Ru**](aq)	454, 484	669[b]
$\mathbf{Mg_2[5Ru]\cdot 19H_2O}$	630[a]	662[c]
$\mathbf{Cd_2[5Ru]\cdot 12H_2O}$	647[a]	688[b]

[a]Wavelength of half-absorption at 500 nm. [b]λ_{ex} = 500 nm. [c]λ_{ex} = 590 nm.

are in the same time scale as those of [**5Ru**] and [**4Ru**] in aqueous solutions (37 and 700 ns), suggesting that these absorption and emission bands are assignable to the ^{1}MLCT absorption and ^{3}MLCT emission of each [***n*Ru**] moiety. The slightly shorter emission lifetime of $(\mathbf{Sr_2[4Ru]\cdot 9H_2O})_2$ than that of [**4Ru**] in the aqueous solution would be due to the heavy-atom effect of the Sr^{2+} ion. Interestingly, the emission maxima of $\mathbf{Mg_2[4Ru]\cdot 13H_2O}$ and $(\mathbf{Sr_2[4Ru]\cdot 9H_2O})_2$ were observed at a longer wavelength of ~50 nm than that of [**4Ru**] in aqueous solution, whereas the emission bands of $\mathbf{Mg_2[5Ru]\cdot 19H_2O}$ and $\mathbf{Cd_2[5Ru]\cdot 12H_2O}$ were observed at wavelengths close to that of [**5Ru**] in aqueous solution. In general, the emission energies of the triplet MLCT transition in ruthenium(II) diimine complexes can be shifted to a lower energy by stabilization of the π^* orbital of the diimine ligand and/or destabilization of the dπ orbital of the Ru^{II} center. Considering the fact that the emission energy of $\mathbf{Mg_2[4Ru]\cdot 13H_2O}$ was shifted to a longer wavelength than that of [**4Ru**] in aqueous solution while the emission energy of $\mathbf{Mg_2[5Ru]\cdot 19H_2O}$ only marginally shifted to a shorter wavelength than that of [**5Ru**] in aqueous solution, the former explanation (stabilization of the π^* orbital of the diimine ligand) does not account for the difference between the $\mathbf{M_2[4Ru]}$ and $\mathbf{M_2[5Ru]}$ systems. One plausible factor is modulation of the electron-donating abilities of the dcbpy ligand by coordination to the M^{2+} cation. Our preliminary molecular orbital (MO) calculations of the metalloligands $[Ru(n,n'\text{-Hdcbpy})_3]^-$ ($[\mathbf{H_3}n\mathbf{Ru}]^-$; n = 4, 5) in which three of six carboxyl groups are protonated suggest that the MOs composed of the dπ orbital of the Ru^{II} ion and the π

dx.doi.org/10.1021/ic402683j | Inorg. Chem. 2014, 53, 2910−2921

orbital of the 4,4′-Hdcbpy$^-$ ligand (HOMO−9, −10, and −11) are delocalized not only on the bpy rings but also on the carboxyl O atoms of the 4,4′-Hdcbpy ligand (Figure S5a in the SI). In contrast, the corresponding MOs of $[\mathbf{H_3 5Ru}]^-$ delocalized only in the bpy rings (Figure S5b in the SI). Thus, coordination to the M^{2+} cation by the carboxyl groups hardly reduced the electron-donating ability of the 5,5′-dcbpy ligand but certainly reduced the ability of the 4,4′-dcbpy ligand. This combination results in a smaller ligand-field splitting between the occupied dπ and unoccupied dσ orbitals, which leads to a red shift of the triplet MLCT emission in the $\mathbf{M_2[4Ru]}$ system. We also checked the change in the luminescence quantum yield (Φ_{em}) of $\mathbf{M_2[4Ru]}$ before and after removal of the crystal water. The yield of dried $\mathbf{Sr_2[4Ru]}$ was estimated to be 1.6% at room temperature and slightly increased to 2.4% by the adsorption of water vapor. In contrast, the yield of dried $\mathbf{Mg_2[4Ru]}$ was found to be 3.7% and slightly decreased to 2.7% by the adsorption of water vapor. These luminescence quantum yields are smaller than that of [**4Ru**] in aqueous solution (Φ_{em} = 6.03%),[25] suggesting that the photoexcited state generated in the $\mathbf{M_2[4Ru]}$ solid state tends to be deactivated more rapidly than that in the solution state. The different behavior between $\mathbf{Mg_2[4Ru]}$ and $\mathbf{Sr_2[4Ru]}$ would be due to the difference in the amounts of adsorbed water molecules in these PCPs.

CONCLUSIONS

We have synthesized five novel luminescent complexes fabricated from two isomeric ruthenium(II) metalloligands $[Ru(n,n'\text{-dcbpy})_3]^{4-}$ ([***n*Ru**]; *n* = 4, 5; *n*,*n*′-dcbpy = *n*,*n*′-dicarboxy-2,2′-bipyridine) and divalent metal ions: $\mathbf{Mg_2[4Ru]\cdot 13H_2O}$, $\mathbf{Mg_2[5Ru]\cdot 19H_2O}$, $(\mathbf{Sr_2[4Ru]\cdot 9H_2O})_2$, $\mathbf{Sr_2[5Ru]\cdot 14H_2O}$, and $\mathbf{Cd_2[5Ru]\cdot 12H_2O}$. Their crystal structures are determined by single-crystal X-ray diffraction. All $\mathbf{M_2[}n\mathbf{Ru]}$ have guest-accessible porous channels with a void fraction ranging from 11.4% for $\mathbf{Mg_2[4Ru]\cdot 13H_2O}$ to 43.9% for $\mathbf{Cd_2[5Ru]\cdot 12H_2O}$. The flexibilities of the porous frameworks strongly depend on the position of the carboxyl group of [***n*Ru**]; $\mathbf{M_2[4Ru]}$ PCPs showing reversible structural transitions accompanied by water or methanol vapor adsorption/desorption; in contrast, the frameworks of $\mathbf{M_2[5Ru]}$ easily and irreversibly collapse by removal of the hydration water molecules present in the porous channels. The absorption and emission properties of the [***n*Ru**] metalloligand in $\mathbf{M_2[}n\mathbf{Ru]}$ are characterized by the same singlet and triplet MLCT transitions as those of [***n*Ru**] in aqueous solution. However, the emission energies also depend on the positions of the carboxyl groups of [***n*Ru**]. Further development of flexible PCPs based on the photofunctional metalloligands is in progress.

ASSOCIATED CONTENT

Supporting Information

X-ray crystallographic data in CIF format of $\mathbf{Mg_2[4Ru]\cdot 13H_2O}$, $(\mathbf{Sr_2[4Ru]\cdot 9H_2O})_2$, $\mathbf{Mg_2[5Ru]\cdot 19H_2O}$, $\mathbf{Sr_2[5Ru]\cdot 14H_2O}$, and $\mathbf{Cd_2[5Ru]\cdot 12H_2O}$, TGA curves of $\mathbf{Mg_2[4Ru]\cdot 13H_2O}$ and $\mathbf{Sr_2[4Ru]\cdot 9H_2O}$, temperature dependence of the IR spectra of $\mathbf{Mg_2[4Ru]\cdot 13H_2O}$ and $(\mathbf{Sr_2[4Ru]\cdot 9H_2O})_2$, PXRD patterns of as-synthesized and dried $\mathbf{Mg_2[5Ru]\cdot 19H_2O}$ and $\mathbf{Cd_2[5Ru]\cdot 12H_2O}$, CO_2 adsorption isotherms of $\mathbf{Mg_2[4Ru]\cdot 13H_2O}$ and $(\mathbf{Sr_2[4Ru]\cdot 9H_2O})_2$ at 194 K, schematic MO diagrams of $[\mathbf{H_3 4Ru}]^-$ and $[\mathbf{H_3 5Ru}]^-$, and selected bond distances of the [***n*Ru**] metalloligand. This material is available free of charge via the Internet at http://pubs.acs.org.

AUTHOR INFORMATION

Corresponding Authors

*E-mail: akoba@sci.hokudai.ac.jp.

*E-mail: mkato@sci.hokudai.ac.jp.

Notes

The authors declare no competing financial interest.

ACKNOWLEDGMENTS

This work is supported by JST-PRESTO, Grant-in-Aid for Scientific Research (B) (Grant 23350025), Coordination Programming (Grant 2107), Artificial Photosynthesis (Grant 2406), Young Scientists (B) (Grant 24750049), and the Global COE Program (Project No. B01: Catalysis as the Basis for Innovation in Materials Science) from MEXT, Japan.

REFERENCES

(1) (a) Kitagawa, S.; Kitaura, R.; Noro, S. *Angew. Chem., Int. Ed.* **2004**, *43*, 2334. (b) Li, H.; Eddaoudi, M.; O'Keeffe, M.; Yaghi, O. M. *Nature* **1999**, *402*, 276. (c) Rosi, N. L.; Eckert, J.; Eddaoudi, M.; Vodak, D. T.; Kim, J.; O'Keeffe, M.; Yaghi, O. M. *Science* **2003**, *300*, 1127.

(2) (a) Dinca, M.; Long, J. R. *Angew. Chem., Int. Ed.* **2008**, *47*, 6766. (b) Navarro, J. A. R.; Barea, E.; Salas, J. M.; Masciocchi, N.; Calli, S.; Sironi, A.; Ania, C. O.; Parra, J. B. *Inorg. Chem.* **2006**, *45*, 2397. (c) Mulfort, K. L.; Hupp, J. T. *Inorg. Chem.* **2008**, *47*, 7936.

(3) (a) Seo, J. S.; Whang, D.; Lee, H.; Jun, S. I.; Oh, J.; Jeon, Y. J.; Kim, K. *Nature* **2000**, *404*, 982. (b) Dybtsev, D. N.; Nuzhdin, A. L.; Chun, H.; Bryliakov, K. P.; Talsi, E. P.; Fedin, V. P.; Kim, K. *Angew. Chem., Int. Ed.* **2006**, *45*, 916.

(4) (a) Lee, C. Y.; Farha, O. K.; Hong, B. J.; Sarjeant, A. A.; Nguyen, S. T.; Hupp, J. T. *J. Am. Chem. Soc.* **2011**, *133*, 15858. (b) Cui, H.; Wang, Z.; Takahashi, K.; Okano, Y.; Kobayashi, H.; Kobayashi, A. *J. Am. Chem. Soc.* **2006**, *128*, 15074. (c) White, K. A.; Chengelis, D. A.; Gogick, K. A.; Stehman, J.; Rosi, N. L.; Petoud, S. *J. Am. Chem. Soc.* **2009**, *131*, 18069. (d) Zucchi, G.; Maury, O.; Thuéry, P.; Ephritikhine, M. *Inorg. Chem.* **2008**, *47*, 10398.

(5) (a) Noro, S.; Kitaura, R.; Kudo, M.; Kitagawa, S.; Ishii, T.; Matsuzaka, H.; Yamashita, M. *J. Am. Chem. Soc.* **2002**, *124*, 2568. (b) Rosi, N. L.; Kim, J.; Eddaoudi, M.; Chen, B.; O'Keeffe, M.; Yaghi, O. M. *J. Am. Chem. Soc.* **2005**, *127*, 1504. (c) Devic, T.; Serre, C.; Audebrand, N.; Marrot, J.; Férey, G. *J. Am. Chem. Soc.* **2005**, *127*, 12788. (d) Koh, K.; Wong-Foy, A. G.; Matzger, A. J. *J. Am. Chem. Soc.* **2009**, *131*, 4184. (e) Zhao, D.; Yuan, D.; Sun, D.; Zhou, H.-C. *J. Am. Chem. Soc.* **2009**, *131*, 9186.

(6) (a) Dinca, M.; Long, J. R. *J. Am. Chem. Soc.* **2005**, *127*, 9376. (b) Zhou, W.; Wu, H.; Yildirim, T. *J. Am. Chem. Soc.* **2008**, *130*, 15268. (c) Kaye, S. S.; Long, J. R. *J. Am. Chem. Soc.* **2008**, *130*, 806. (d) Lee, W. R.; Ryu, D. W.; Lee, J. W.; Yoon, J. H.; Koh, E. K.; Hong, C. S. *Inorg. Chem.* **2010**, *49*, 4723.

(7) (a) Hasegawa, S.; Horike, S.; Matsuda, R.; Furukawa, S.; Mochizuki, K.; Kinoshita, Y.; Kitagawa, S. *J. Am. Chem. Soc.* **2007**, *129*, 2607. (b) Shultz, A. M.; Farha, O. K.; Hupp, J. T.; Nguyen, S. T. *J. Am. Chem. Soc.* **2009**, *131*, 4204.

(8) (a) Halder, G. J.; Kepert, C. J.; Moubaraki, B.; Murray, K. S.; Cashion, J. D. *Science* **2002**, *298*, 1762. (b) Halder, G. J.; Kepert, C. J. *J. Am. Chem. Soc.* **2005**, *127*, 7891. (d) Horike, S.; Shimomura, S.; Kitagawa, S. *Nat. Chem.* **2009**, *1*, 695. (c) Fukushima, T.; Horike, S.; Inubushi, Y.; Nakagawa, K.; Kubota, Y.; Takata, M.; Kitagawa, S. *Angew. Chem., Int. Ed.* **2010**, *49*, 4820.

(9) Chandler, B. D.; Cramb, D. T.; Shimizu, G. K. H. *J. Am. Chem. Soc.* **2006**, *128*, 10403.

(10) Kitaura, R.; Onoyama, G.; Sakamoto, H.; Matsuda, R.; Noro, S.; Kitagawa, S. *Angew. Chem., Int. Ed.* **2004**, *43*, 2684.

(11) (a) Kent, C. A.; Mehl, B. P.; Ma, L.; Papanikolas, J. M.; Meyer, T. J.; Lin, W. *J. Am. Chem. Soc.* **2010**, *132*, 12767. (b) Kent, C. A.; Liu, D.; Meyer, T. J.; Lin, W. *J. Am. Chem. Soc.* **2012**, *134*, 3991.

(12) (a) Kalyanasundaram, K. *Photochemistry of Polypyridine and Porphyrin Complexes*; Academic Press: London, 1992. (b) Juris, A.; Balzani, V.; Barigelletti, F.; Campagna, S.; Belser, P.; Zelewsky, A. V. *Coord. Chem. Rev.* **1988**, *84*, 85. (c) Nazeeruddin, Md. K.; Kalyanasundaram, K. *Inorg. Chem.* **1989**, *28*, 4251.
(13) (a) Uddin, Md. J.; Yoshimura, A.; Ohno, T. *Bull. Chem. Soc. Jpn.* **1999**, *72*, 989. (b) Yoshimura, A.; Nozaki, K.; Ohno, T. *Coord. Chem. Rev.* **1997**, *159*, 375.
(14) (a) Hayami, S.; Murata, K.; Urakami, D.; Kojima, Y.; Akita, M.; Inoue, K. *Chem. Commun.* **2008**, 6510. (b) Hayami, S.; Urakami, D.; Kojima, Y.; Yoshizaki, H.; Yamamoto, Y.; Kato, K.; Fuyuhiro, A.; Kawata, S.; Inoue, K. *Inorg. Chem.* **2010**, *49*, 1428.
(15) (a) Masaoka, S.; Sakai, K. *Chem. Lett.* **2009**, *38*, 182. (b) Concepcion, J. J.; Jurss, J. W.; Norris, M. R.; Chen, Z.; Templeton, J. L.; Meyer, T. J. *Acc. Chem. Res.* **2009**, *42*, 1954. (c) Krishnan, C. V.; Brunschwig, B. S.; Creutz, C.; Sutin, N. *J. Am. Chem. Soc.* **1985**, *107*, 2005.
(16) Kobayashi, A.; Suzuki, Y.; Ohba, T.; Noro, S.; Chang, H.-C.; Kato, M. *Inorg. Chem.* **2011**, *50*, 2061.
(17) Eskelinen, E.; Luukkanen, S.; Haukka, M.; Ahlgrén, M.; Pakkanen, T. A. *J. Chem. Soc., Dalton Trans.* **2000**, 2745.
(18) Matthews, C. J.; Elsegood, M. R. J.; Bernardinelli, G.; Clegge, W.; Williams, A. F. *Dalton Trans.* **2004**, 492.
(19) *CrystalClear*; Molecular Structure Corp.: Orem, UT, 2001.
(20) *SIR2004*: Burla, M. C.; Caliandro, R.; Camalli, M.; Carrozzini, B.; Cascarano, G. L.; De Caro, L.; Giacovazzo, C.; Polidori, G.; Spagana, R. *J. Appl. Crystallogr.* **2005**, *38*, 381.
(21) *SHLEX97*: Sheldrick, G. M. *Acta Crystallogr., Sect. A* **2008**, *64*, 112.
(22) *CrystalStructure 4.0*; *Crystal Structure Analysis Package*; Rigaku Corp.: Tokyo, Japan, 2000.
(23) *Platon SQUEEZE*: Spek, A. L. *J. Appl. Crystallogr.* **2003**, *36*, 7.
(24) Rockland, L. B. *Anal. Chem.* **1960**, *32*, 1375.
(25) Suzuki, K.; Kobayashi, A.; Kaneko, S.; Takehira, K.; Yoshihara, T.; Ishida, H.; Shiina, Y.; Oishi, S.; Tobita, S. *Phys. Chem. Chem. Phys.* **2009**, *11*, 9850.